EPiC Series in Computing

Volume 114, 2026, Pages 101–114

Proceedings of the Workshop on Mathematical Modeling and Scientific Computing

Machine Learning-Based Polynomial Surrogate Model for Calibrating Effective Wall Slip in Microvessel Blood Flow Simulations

Andrey Kovtanyuk[1,2] and Petr Andriushchenko[3]

[1] Far Eastern Center for Research and Education in Mathematics,
Far Eastern Federal University, Vladivostok, Russia
kovtanyuk.ae@dvfu.ru

[2] School of Computation, Information and Technology,
Technical University of Munich, Munich, Germany
kovtanyu@ma.tum.de

[3] Heidelberg Institute of Global Health,
Heidelberg University, Heidelberg, Germany
petr.andriushchenko@iwr.uni-heidelberg.de

Abstract

A polynomial surrogate model developed within a supervised machine learning framework is proposed for calibrating an effective slip boundary condition in finite-element models of blood flow in microvessels with diameters of $4-8$ μm. Blood is represented as a two-phase fluid with spatially varying viscosity, and the wall-slip coefficient α is determined by matching the finite-element apparent viscosity to an empirical *in vitro* apparent-viscosity relation. The calibration was performed over a three-dimensional parameter space defined by the vessel radius, linear hematocrit, and cell-free-layer thickness. A finite viscosity-matching value of α was obtained for 105 of the 125 investigated geometries, whereas for 20 geometries the empirical target could not be reached even in the no-slip limit. The dimensionless slip parameter was represented by a cubic response surface, yielding $R^2 = 0.9998$ and a five-fold cross-validated $R^2 = 0.9996$. The resulting surrogate model provides an efficient representation of the calibrated boundary condition within the sampled feasible parameter domain.

1 Introduction

Realistic simulation of blood circulation in a vascular system requires an adequate mathematical description of blood flow in a single vessel. Assuming that the blood is a homogeneous and incompressible fluid, we can describe its flow by the following Poiseuille's law [16]:

$$Q = \frac{\Delta p}{R} := \frac{\pi}{8}\frac{r^4}{L\mu}\Delta p. \tag{1}$$

Here, Q is the blood flow rate, Δp the pressure difference (pressure drop), R the resistance of the vessel, r the radius of the vessel, L the length of the vessel, μ the fluid viscosity. Poiseuille's law

V. Turova, A. Kovtanyuk, A. Maslovskaya and J. Zimmer (eds.), MMSC 2026 (EPiC Series in Computing, vol. 114), pp. 101–114

provides an adequate description of blood flow in vessels with sufficiently large diameters. For microvessels, e.g., for capillaries, the blood cannot be considered as a homogeneous fluid with a constant viscosity. Instead, it is considered as a two-phase fluid consisting of plasma and RBCs, wherein the RBC phase has much higher viscosity compared to the plasma phase. Note that under the simplifying assumption of the homogeneity of the central zone filled with erythrocytes (see N.D. Botkin et al. [1]), this approach makes it possible to obtain an analytical expression for the blood flow velocity in the capillary. Then, N.D. Botkin et al. [2] calculated the blood flow velocity based on the Stokes equations for the case of variable viscosity, accounting for the size and shape of erythrocytes as well as the hematocrit level. Subsequently, this approach was extended by A.E. Kovtanyuk et al. [9, 10] to choose appropriate boundary conditions to obtain consistency between the numerical results and experimental data.

Although Poiseuille's law does not apply to microvessels, to evaluate resistance to blood flow in the capillaries, it is possible, based on equality (1), to define the apparent viscosity of the blood, that is, the viscosity of a homogeneous fluid that provides the same blood flow rate for a given capillary radius, capillary length, and pressure drop. According to (1), the apparent viscosity is determined as

$$\mu_{\text{app}} = \frac{\pi}{8} \frac{r_{\text{c}}^4}{L} \frac{\Delta p}{Q}\,, \tag{2}$$

where r_{c} is the radius of a capillary.

The application of formula (2) to microvessels requires modeling blood flow while accounting for its heterogeneous structure. Numerous studies have addressed this topic (see, e.g., [12, 13, 14, 17]). Currently, research into microvascular blood flow continues, utilizing both continuum-based approaches and methods that explicitly account for individual cells. In this context, particular attention is paid to the role of red blood cell transport, the formation of a cell-free marginal layer, and the spatial heterogeneity of the hematocrit in determining flow resistance and effective viscosity [3, 6, 8, 15].

Experimental measurements of the apparent viscosity are performed *in vitro* and *in vivo*. Usually, *in vitro* data correspond to blood flow in glass tubes, whereas *in vivo* data are obtained from microvessels of animals. In the case of blood vessels with a relatively large diameter, the observed behaviour of the apparent blood viscosity is similar to that in glass tubes. However, for microvessels there is a significant difference between *in vitro* and *in vivo* measurements [13, 14].

The dependence of the apparent viscosity on the discharge hematocrit and vessel diameter and corresponding analytical approximations, both *in vitro* and *in vivo*, was established by T.W. Secomb and A.R. Pries [16, 17]. Comparative analysis of the formulas for the apparent viscosity in microvessels shows that the *in vivo* values are significantly greater than *in vitro* values for capillary diameters, that is, for diameters smaller than 8μm. The observed significant difference between the *in vivo* and *in vitro* data can be explained by the presence of the endothelial surface layer (ESL), which is located between the vascular endothelium and blood and is characterized by a significantly retarded plasma motion. A.L. Copley studied the endothelium-plasma interface and developed a concept that assumes the presence of an immobile layer of plasma at the vessel wall [4, 5]. In the paper [10], the influence of the immobile plasma boundary layer on the apparent viscosity is studied. Calculating the blood flow Q for a given pressure drop Δp, the authors compare the apparent viscosity obtained using the formula (2) with *in vivo* data from [17]. The closeness of the results of the mathematical modeling to *in vivo* data is achieved by choosing the corresponding thickness of the immobile plasma boundary layer. Note that a significant difference between *in vitro* data and the results of the finite element modeling is observed if a no-slip boundary condition for the velocity at the vessel

wall is used. A possible way to match the results of numerical simulation with experimental data is to use the slip boundary condition for the longitudinal component of the velocity.

The study [9] examines an approach similar to that in [10] for approximating *in vivo* data, and also reproduces the *in vitro* data from [17] by selecting an appropriate vessel-wall slip coefficient. It should be noted that the approaches employed in [9] and [10] were based on additional assumptions regarding the relationship between the vessel radius and the thickness of the erythrocyte-free plasma layer at the vessel wall. A more general approach, without additional assumptions, increases the number of uncertain parameters and, consequently, the complexity of the problem.

Building on these studies, the present work considers a more general formulation in which vessel radius, linear hematocrit, and cell-free-layer thickness are treated as independent model parameters, without imposing an additional relationship between vessel radius and cell-free-layer thickness. For each parameter combination, the effective vessel-wall slip coefficient α is calibrated by matching the apparent viscosity obtained by the finite-element modeling to an empirical *in vitro* apparent-viscosity relation. The resulting calibrated values are then used to construct a polynomial response surface surrogate model describing the relationship between the model parameters and the effective slip coefficient. This framework also makes it possible to identify regions of the parameter space in which the empirical viscosity target cannot be reproduced even in the no-slip limit.

2 Finite element modeling

2.1 Stokes equations with spatially varying viscosity

As proposed by N.D. Botkin et al. in [2], blood and plasma are represented as a single flow field with spatially varying viscosity, with the effective viscosity in the RBC region taken to be approximately 100 times the plasma viscosity.

Further, we assume that the flow is steady-state and without transition effects. Therefore, the blood flow in a capillary can be described by the steady-state Stokes equations with spatially varying viscosity. Assuming that the flow is axisymmetric, all variables depend on the radial x_1 and longitudinal x_2 coordinates only. Let u_1 and u_2 be the radial and longitudinal flow velocities, respectively, and p the pressure. Therefore, we come to the consideration of the two-dimensional computational domain Ω,

$$\Omega = \{(x_1, x_2) \in (0, r_c) \times (0, L)\},$$

presented in cylindrical coordinates (see Fig. 1). Here, r_c is the radius of the capillary, r_e is the radius of RBCs, l is the thickness of RBCs, and l_0 is the thickness of the plasma layer between two adjacent RBCs. The parameter h describes the deformation of the RBC, the leading part of which (in the direction of motion) is described by a quadratic function. Here, we assume that parameters l, l_0, and h are constants for all domain.

For the velocity $u = (u_1, u_2)$ and pressure p, the corresponding Stokes equations in the domain Ω have the form:

$$-2\nabla \cdot (\mu \mathbf{D}(u)) + \nabla p = 0, \tag{3}$$

$$\nabla \cdot u = 0. \tag{4}$$

Here, $\nabla \cdot u$ is the velocity divergence and $\mathbf{D}$ is the velocity deformation tensor, which, in cylindrical coordinates and accounting for axial symmetry, are defined as

$$\nabla \cdot u = u_1/x_1 + \partial u_1/\partial x_1 + \partial u_2/\partial x_2$$

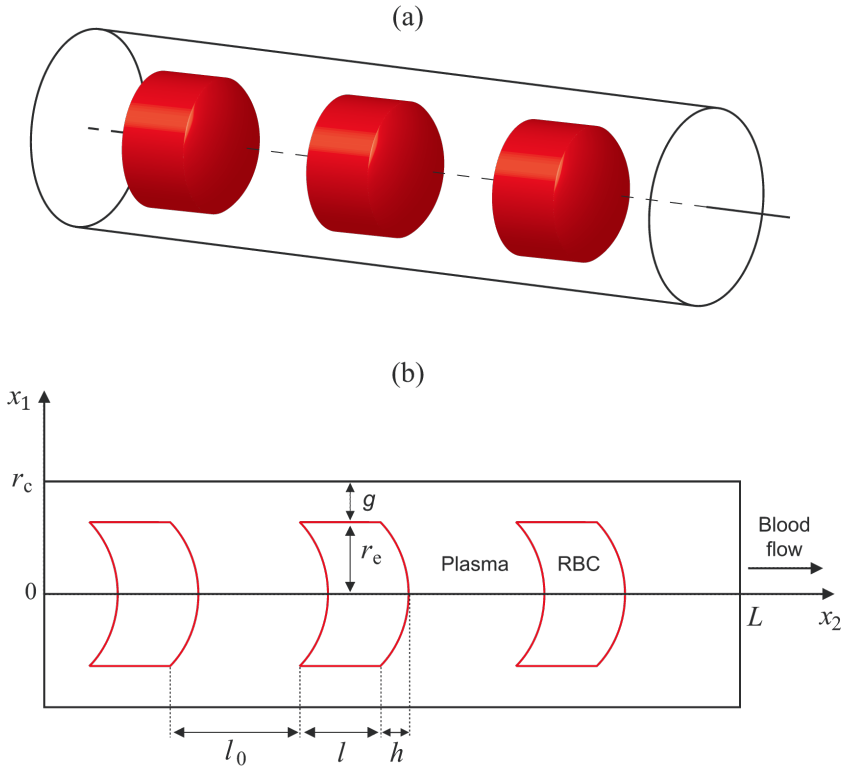


Figure 1: Scheme of the domain: (a) 3D scheme, (b) longitudinal cross-section. Here r_c is the capillary radius, r_e is the RBCs radius, l is the RBCs thickness, l_0 is the thickness of the plasma layer between two adjacent RBCs, h is the RBC deformation, g is the cell-free layer (CFL) thickness, L is the calculation domain length

and

$$\mathbf{D}(u) = \frac{1}{2}\begin{pmatrix} 2\partial u_1/\partial x_1 & 0 & \partial u_1/\partial x_2 + \partial u_2/\partial x_1 \\ 0 & 2u_1/x_1 & 0 \\ \partial u_1/\partial x_2 + \partial u_2/\partial x_1 & 0 & 2\partial u_2/\partial x_2 \end{pmatrix}.$$

To formulate the boundary conditions, the following parts of the boundary $\partial\Omega$ of the domain Ω are determined:

$$\Gamma_0 = \{x \in \partial\Omega : x_1 = r_c\}, \quad \Gamma_1 = \{x \in \partial\Omega : x_2 = 0\}, \quad \Gamma_2 = \{x \in \partial\Omega : x_2 = L\}.$$

Further, Equations (3) and (4) are supplemented by the following boundary conditions at the boundaries Γ_1 and Γ_2:

$$u_1|_{\Gamma_1} = u_1|_{\Gamma_2} = 0, \tag{5}$$

$$p|_{\Gamma_1} = p_0, \quad p|_{\Gamma_2} = 0. \tag{6}$$

The boundary conditions at the boundary Γ_0 depend on the type of vessel. In the case of vessels containing an endothelial layer, a retardation of blood flow occurs in the near-wall region, such that the most appropriate boundary condition is zero velocity at the vessel wall,

$$u|_{\Gamma_0} = 0. \tag{7}$$

Moreover, when modeling the endothelial layer, it is often assumed that the blood velocity is zero within a certain near-wall layer. Consequently, the modeling of blood flow is performed using a vessel of smaller diameter, referred to as the effective diameter. In this regard, we assume that the boundary Γ_0 specified in the boundary conditions (7) is defined by the effective diameter, which may be smaller than the anatomical diameter.

When modeling blood flow in glass tubes (*in vitro* modeling), slip conditions are more appropriate for the component u_2,

$$u_1\big|_{\Gamma_0} = 0, \tag{8}$$

$$\frac{\partial u_2}{\partial x_1} + \alpha u_2\big|_{\Gamma_0} = 0, \tag{9}$$

where α is the slip coefficient. The corresponding slip length is $\beta = 1/\alpha$.

The problem (3)–(7) is typical for *in vivo* modeling, and the problem (3)–(6), (8)–(9) is typical for *in vitro* modeling.

Note that due to equalities (4) and (5), the following conditions on the component u_2 at the boundaries Γ_1 and Γ_2 hold:

$$\frac{\partial u_2}{\partial x_2}\Big|_{\Gamma_1} = \frac{\partial u_2}{\partial x_2}\Big|_{\Gamma_2} = 0.$$

2.2 Weak forms of the Stokes equations

To obtain weak forms of problem (3)–(7) and problem (3)–(6), (8)–(9), we introduce the spaces V_1, V_2, and Q such that

$$V_1 = \{v \in \mathcal{D}' :\ x_1^{-1/2} v \in L^2(\Omega),\ x_1^{1/2}\partial v/\partial x_i \in L^2(\Omega),\ i = 1,2\},$$

$$V_2 = \{v \in \mathcal{D}' :\ x_1^{1/2} v \in L^2(\Omega),\ x_1^{1/2}\partial v/\partial x_i \in L^2(\Omega),\ i = 1,2\},$$

$$Q = \{q \in \mathcal{D}' :\ x_1^{1/2} q \in L^2(\Omega)\},$$

where $\mathcal{D}'$ is the space of distributions on Ω.

Then, we consider the space

$$V = \{v = (v_1, v_2) \in V_1 \times V_2,\ v|_{\Gamma_0} = 0,\ v_1|_{\Gamma_1} = v_1|_{\Gamma_2} = 0\}$$

and define the weak form of the problem (3)–(7).

Weak form (A):

For $u \in V$, $p \in Q$, the weak form of problem (3)–(7) consists of the following equations

$$\int\limits_{\Omega} \Big(2x_1\,\mu\,\mathbf{D}(u)\mathbf{D}(v) - x_1\,p\,\nabla\cdot v\Big)dx - \int\limits_{\Gamma_1} p_0\,x_1\,v_2\,dx = 0 \quad \forall v \in V, \tag{10}$$

$$\varepsilon \int\limits_{\Omega} x_1 p\,q\,dx - \int\limits_{\Omega} x_1 \nabla\cdot u\,q\,dx = 0 \qquad \forall q \in L^2(\Omega), \quad \varepsilon \ll 1, \tag{11}$$

supplemented by the boundary conditions (5)–(7). Here, the term multiplied by ε is added to ensure numerical stability of the solution.

To write a weak form of the problem (3) – (6), (8) – (9), we introduce the space

$$W = \{v = (v_1, v_2) \in V_1 \times V_2,\ v_1|_{\Gamma_0} = v_1|_{\Gamma_1} = v_1|_{\Gamma_2} = 0\}.$$

Then, we come to the following weak form of problem (3) – (6), (8) – (9).

Weak form (B):

For $u \in W$, $p \in Q$, the weak form of problem (3) – (6), (8) – (9) consists of the following equations

$$\int\limits_{\Omega} \Big(2x_1\,\mu\,\mathbf{D}(u)\mathbf{D}(v) - x_1\,p\,\nabla\cdot v\Big)dx + \int\limits_{\Gamma_0} x_1\mu\,\alpha\,u_2\,v_2\,dx - \int\limits_{\Gamma_1} p_0\,x_1\,v_2\,dx = 0 \quad \forall v \in W, \tag{12}$$

$$\varepsilon \int\limits_{\Omega} x_1 p\,q\,dx - \int\limits_{\Omega} x_1 \nabla\cdot u\,q\,dx = 0 \qquad \forall q \in L^2(\Omega), \quad \varepsilon \ll 1, \tag{13}$$

supplemented by the boundary conditions (5), (6), and (8).

The weak formulations obtained for the problem form the basis for applying the Finite Element Method. For its implementation, FreeFEM++ package is used [7]. When performing numerical simulations, P2 finite element space is utilized for the approximation of the functions u and v, whereas P1 finite element space is used for the approximation of the functions p and q. The length L of the calculation domain was determined by the sum of the thicknesses of two RBCs and two layers of plasma between adjacent RBCs, that is, $L = 2l + 2l_0$. The thickness l of RBC is determined by its mean volume equal to 88 μm^3 [11] and the value of the RBC radius r_{e}, that is $l = 88/\pi r_{\mathrm{e}}^2$ (units in μm). Taking into account that the results of finite element modeling are stable with respect to RBC deformation [2], we used the deformation parameter $h = l/3$. The sides of the computational domain were discretized with a step of approximately 0.1 μm, the viscosity distribution μ is equal to 0.001 Pa $\cdot$ s in the plasma part and 0.1 Pa $\cdot$ s in the RBCs part, and the parameter $\varepsilon = 10^{-8}$. A constant axial pressure gradient [10] was used in all simulations

$$G = \frac{p_0}{L} = 5/3\,(\mathrm{Pa}\cdot\mu\mathrm{m}^{-1}). \tag{14}$$

Accordingly, the applied pressure difference was adjusted to the length of computational-domain according to

$$p_0 = GL. \tag{15}$$

Thus, although the value L depends on the linear hematocrit and the RBC geometry, the applied pressure gradient remains the same for all combinations of parameters.

3 Fitting the results of the finite element modeling to experimental data

Solving the Stokes equation problems presented in the previous section requires specifying a number of parameters. Some of these can be measured, whereas for others, there are no explicit formulas or clear relationships. Measurable parameters include the radius of the vessel r_{c} and the linear hematocrit H, where

$$H = l/(l + l_0).$$

Parameters that are uncertain for the weak formulation (A) include the effective vessel radius (i.e., the radius excluding the immobile plasma wall layer) and the thickness g of the cell-free layer (CFL),

$$g = r_{\mathrm{c}} - r_{\mathrm{e}}\,.$$

The above-mentioned measurable and uncertain parameters determine the RBC boundary, that is, the variable viscosity.

The uncertain parameters in the weak problem (B) are the thickness g of the CFL and the slip coefficient α. In the calculations below, g is treated as an input parameter, while α is calibrated so that the apparent viscosity obtained from the finite element modeling agrees with the experimental *in vitro* data reported in [17].

FEM calculations were performed in SI units, with the parameter α in m^{-1}, but here we report it in $\mu\mathrm{m}^{-1}$.

3.1 Viscosity-matching criterion

For each finite element solution, the total flow rate Q is calculated from the longitudinal velocity field,

$$Q = 2\pi \int_0^{r_{\mathrm{c}}} u_2(x_1, L) x_1 dx_1. \tag{16}$$

The rate of blood flow through the central area, where RBCs move, is denoted as Q_{e},

$$Q_{\mathrm{e}} = 2\pi \int_0^{r_{\mathrm{e}}} u_2(x_1, x_2') x_1 dx_1. \tag{17}$$

Here, the cross-section $x_2 = x_2'$ passes through an RBC.

Then, the discharge hematocrit is evaluated as

$$H_D = \frac{H Q_{\mathrm{e}}}{Q}. \tag{18}$$

The apparent viscosity obtained from the finite element solution is calculated using (2). The viscosity is then normalized by the plasma viscosity $\mu_1 = 0.001\,\mathrm{Pa}\cdot\mathrm{s}$, such that

$$\widetilde{\mu} = \frac{\pi r_{\mathrm{c}}^4}{8L} \frac{p_0}{Q\mu_1} \tag{19}$$

is the relative apparent viscosity. It should be noted that the relative apparent viscosity may depend on several parameters, including the slip coefficient α, that is, $\widetilde{\mu} = \widetilde{\mu}(\alpha)$.

For the comparison with *in vitro* data, we use the analytical approximation of the relative apparent viscosity $\widetilde{\mu}_{\mathrm{vitro}}$ from [17]. Let $D = 2r_{\mathrm{c}}$ be the tube diameter in μm and

$$A = \frac{1}{1 + 10^{-11} D^{12}}, \qquad C = (0.8 + \exp(-0.075D))\,(A - 1) + A, \tag{20}$$

$$\mu_{0.45} = 220\exp(-1.3D) + 3.2 - 2.44\exp\left(-0.06D^{0.645}\right). \tag{21}$$

Then the target *in vitro* relative apparent viscosity is determined as

$$\widetilde{\mu}_{\mathrm{vitro}} = 1 + (\mu_{0.45} - 1)\big((1 - H_D)^C - 1\big)\big((1 - 0.45)^C - 1\big)^{-1}. \tag{22}$$

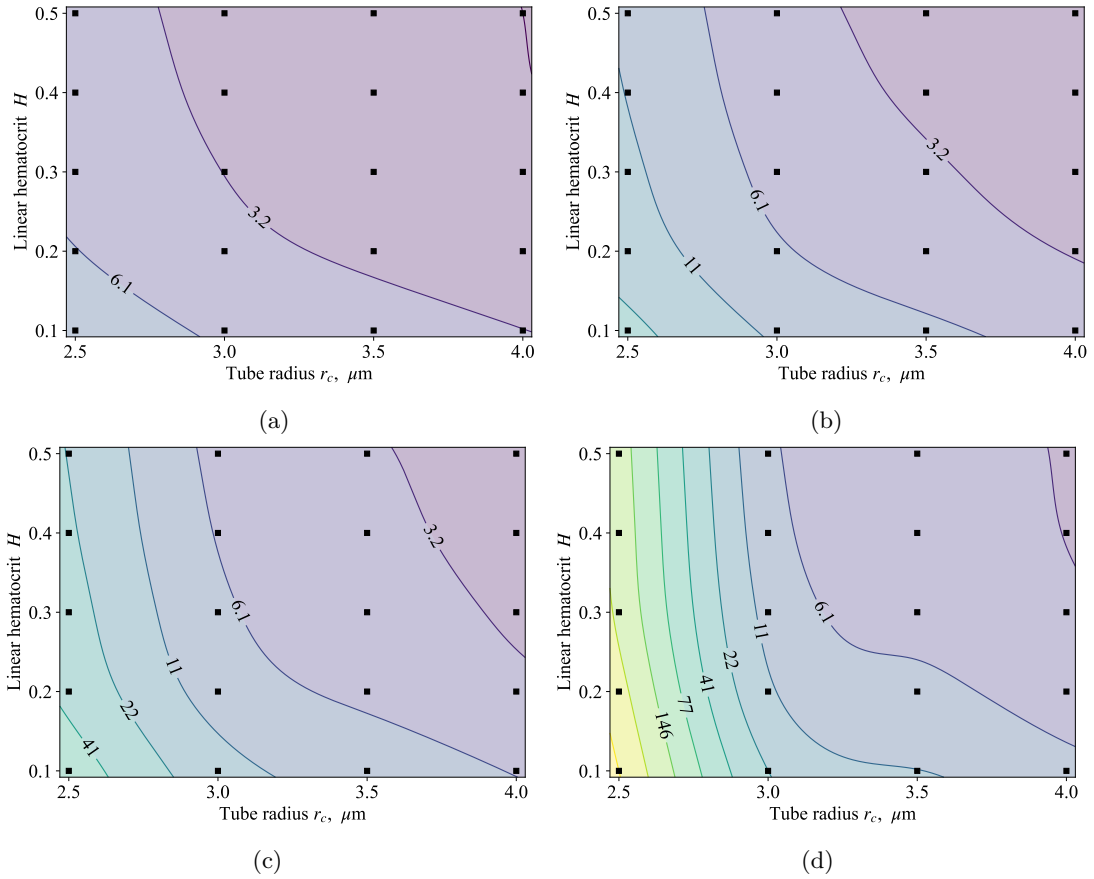


Figure 2: Behavior of the slip coefficient α (units in μm^{-1}) as a function of linear hematocrit H and vessel radius r_c for the following thickness of the cell-free layer g: (a) $0.1\,\mu$m; (b) $0.3\,\mu$m; (c) $0.4\,\mu$m; (d) $0.5\,\mu$m. The black dots correspond to values used to construct the regression formula.

For a fixed set (r_c, H, g), the difference between the numerical and experimental viscosities is measured by

$$E(\alpha) = \ln\left(\widetilde{\mu}/\widetilde{\mu}_{\text{vitro}}\right). \tag{23}$$

Thus, the viscosity-matching value α_0 is defined by

$$E(\alpha_0) = 0. \tag{24}$$

Increasing α_0 reduces the longitudinal slip at the glass wall. The total flow rate therefore decreases and the apparent viscosity increases. This behaviour was observed numerically for every parameter combination considered here: $E(\alpha)$ was strictly increasing with α. Consequently, when a zero crossing exists, the viscosity-matching value α_0 is unique.

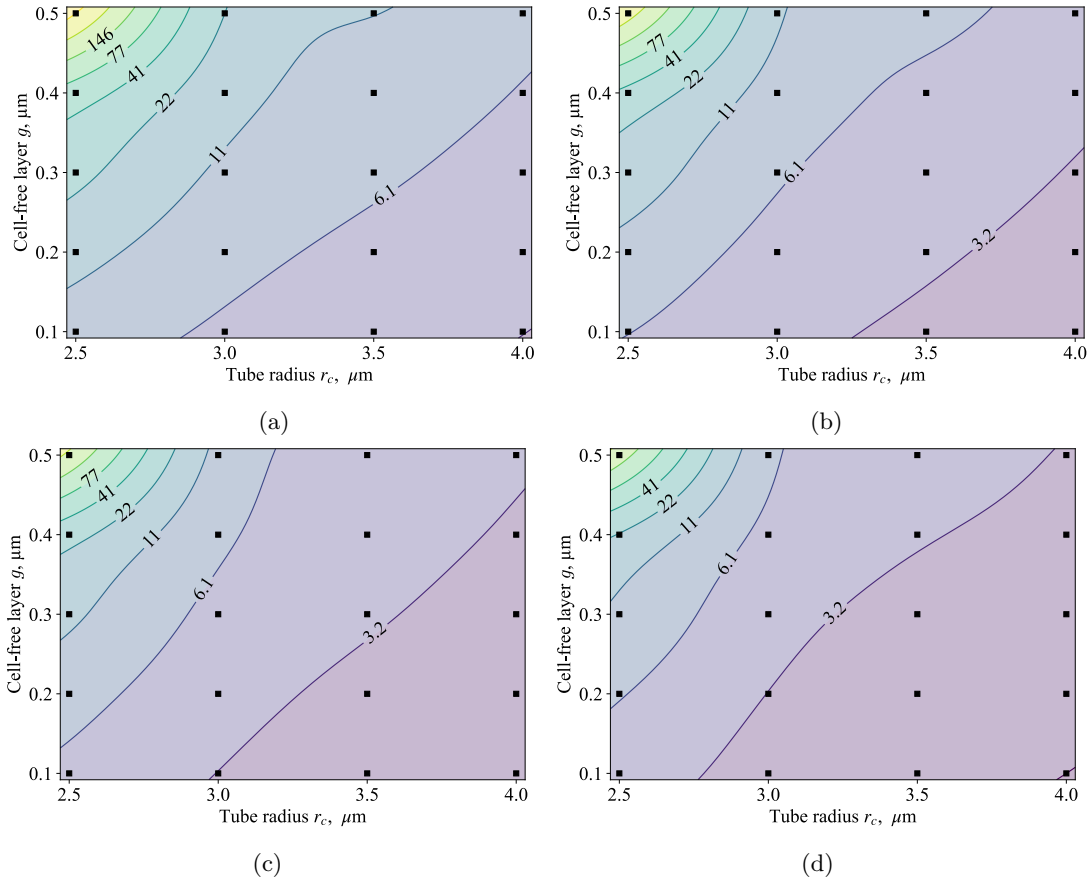


Figure 3: Behavior of the slip coefficient α (units in μm^{-1}) as a function of thickness of the cell-free layer g and vessel radius r_c for the following values of linear hematocrit H: (a) 0.1; (b) 0.2; (c) 0.3; (d) 0.5. The black dots correspond to values used to construct the regression formula.

3.2 Numerical determination of the slip coefficient

The main parametric study was performed on the grid $(r_\text{c},\, g,\, H) \in G_1 \times G_2 \times G_3$, where

$$G_1 = \{2,\, 2.5,\, 3,\, 3.5,\, 4\}\ (\mu\text{m}),$$

$$G_2 = \{0.1,\, 0.2,\, 0.3,\, 0.4,\, 0.5\}\ (\mu\text{m}),$$

$$G_3 = \{0.1,\, 0.2,\, 0.3,\, 0.4,\, 0.5\}.$$

The initial set G_α of parameter α values is determined as

$$G_\alpha = \{1,\, 2,\, 4,\, 8,\, 16,\, 32,\, 80\}\ (\mu\text{m}^{-1}).$$

This gives 125 different geometries and 875 finite element calculations in the initial parametric study.

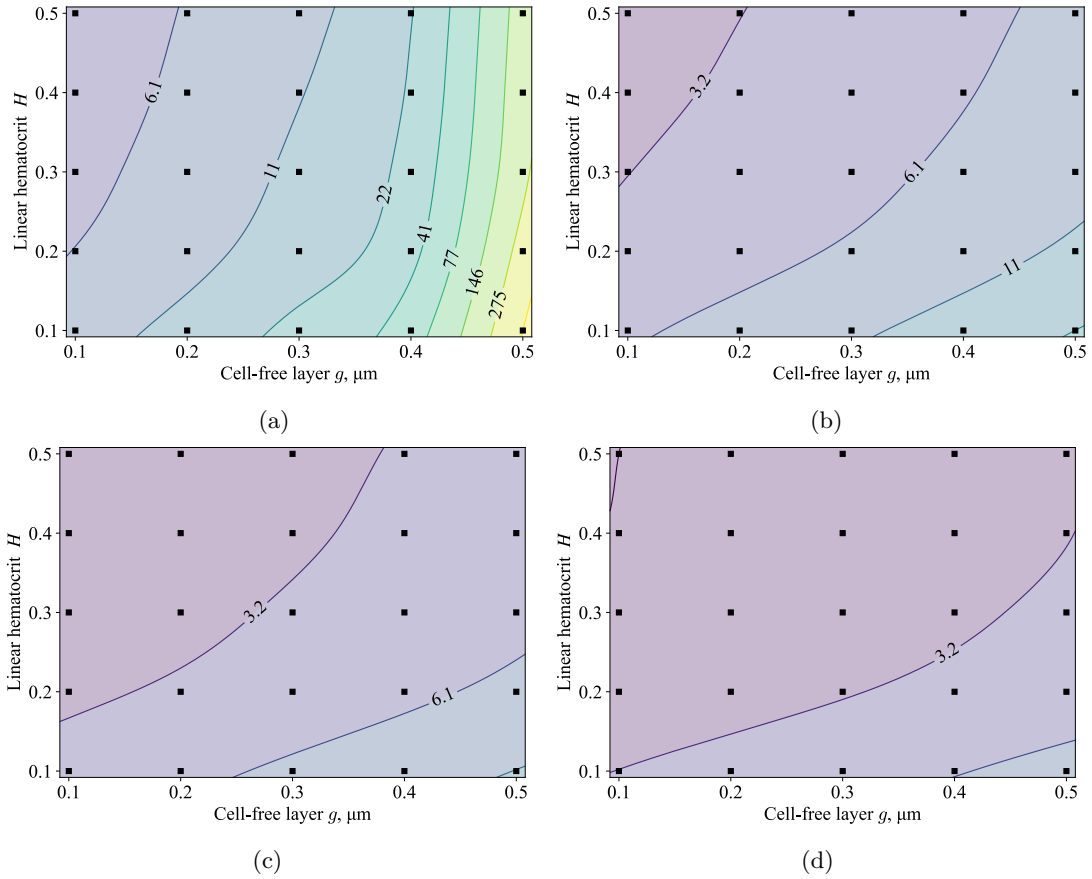


Figure 4: Behavior of the slip coefficient α (units in μm^{-1}) as a function of linear hematocrit H and thickness of the cell-free layer g for the following vessel radius r_c: (a) $2.5\,\mu$m; (b) $3\,\mu$m; (c) $3.5\,\mu$m; (d) $4\,\mu$m. The black dots correspond to values used to construct the regression formula.

A change of sign of E was found within this range for 100 geometries. For the remaining 25 geometries, E was still negative at $\alpha = 80\,\mu\text{m}^{-1}$, so an additional limiting calculation was performed with the no-slip condition $u_2|_{\Gamma_0} = 0$ (the case of $\alpha \to \infty$).

The no-slip calculations separated the 25 cases into two groups. For

$$r_c = 2\,\mu\text{m}; \qquad g = 0.2\,\mu\text{m},\ 0.3\,\mu\text{m},\ 0.4\,\mu\text{m},\ 0.5\,\mu\text{m},$$

the FEM apparent viscosity remained below the experimental value for all five hematocrit levels. Hence, no finite positive value of α can satisfy (24) for these 20 parameter combinations.

The other five cases were obtained for $r_c = 2.5\,\mu$m and $g = 0.5\,\mu$m. Here the no-slip residual was positive. Additional calculations at

$$\alpha = 160\,\mu\text{m}^{-1},\ 240\,\mu\text{m}^{-1},\ 400\,\mu\text{m}^{-1},\ 600\,\mu\text{m}^{-1},$$

were sufficient to bracket all five roots. The resulting values decrease from approximately $518\,\mu\text{m}^{-1}$ at $H = 0.1$ to $194\,\mu\text{m}^{-1}$ at $H = 0.5$. These cases are already very close to the no-slip limit: the corresponding slip lengths are only about 1.9 – 5.2 nm.

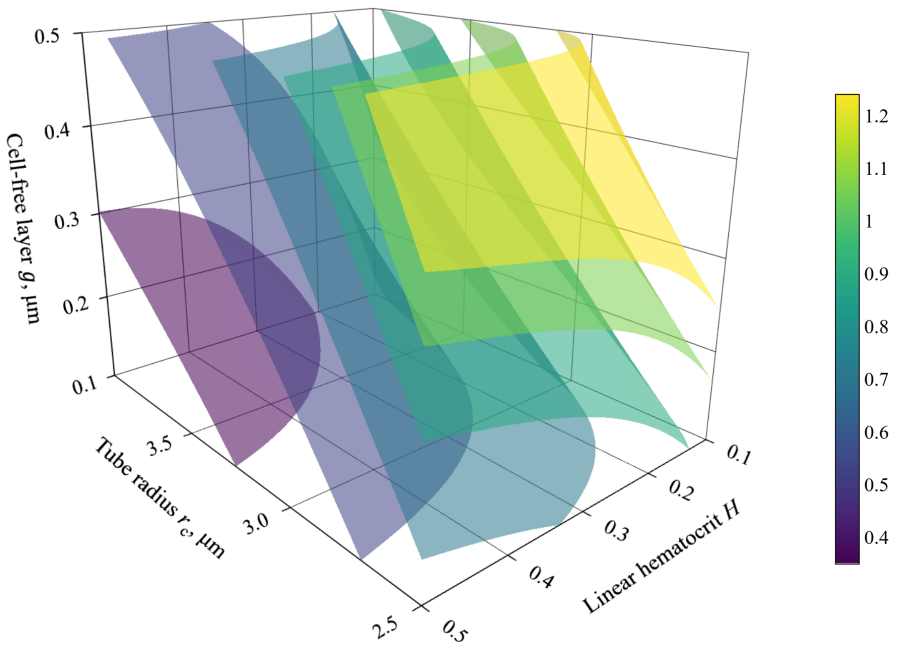


Figure 5: Three-dimensional selected isosurfaces of the effective wall-slip coefficient α predicted by the cubic response-surface model in the parameter space of tube radius r_c, linear hematocrit H, and cell-free-layer thickness g. Each surface represents a constant value of $\log_{10}(\alpha/1\mu\text{m}^{-1})$, with colour indicating the corresponding isosurface level.

It should be noted that the absence of optimal values of α for small r_c and certain values of g is consistent with practical observations, in which the CFL thickness decreases with decreasing vessel radius. Also, when conducting numerical modeling of blood flow in microvessels in [1, 9], the relation $r_e = 0.8r_c + 0.3$ (units in μm) was used, which yields $g = 0.1\,\mu\text{m}$ at $r_c = 2\,\mu\text{m}$.

Altogether, a finite viscosity-matching solution was obtained for 105 of the 125 sampled geometries. The calibrated slip coefficient α_0 covered a wide range from 1.7 μm^{-1} to 518.3 μm^{-1}. Across the feasible part of the grid, the dependence was regular. The value of α_0 decreased as r_c increased, decreased with increasing H, and increased with the CFL thickness g. No violation of these trends was found on the sampled grid.

For each geometry, the value α_0 corresponding to $E(\alpha_0) = 0$ was first estimated from the FEM-computed values of $E(\alpha)$. Once a sign change in $E(\alpha)$ had been bracketed by two neighboring FEM points, a cubic interpolation within this interval was used to obtain a preliminary estimate of α_0. The resulting estimates of α_0 were checked by direct FEM validation calculations. One additional FEM calculation was performed directly at the estimated root for each of the 105 feasible geometries. The mean absolute viscosity mismatch was 0.039%, the median was 0.036%, and the largest mismatch was 0.136%. For all 105 cases the error was below 0.2%. These calculations confirm that the interpolated zero crossings reproduce the target apparent viscosity with sufficient accuracy for the subsequent regression step.

The contour maps shown in Figs. 2–4 are constructed directly from these FEM-calibrated values. The contour lines interpolate between neighboring nodes of the sampled grid. The regression model described below was fitted separately to the 105 finite roots.

Table 1: Coefficients of the cubic response surface (26). The coefficient of the term $r_c^i H^j g^k$ has units $1/\mu m^{i+k}$, which ensures that B is dimensionless.

Term	Coefficient	Term	Coefficient
Intercept	−0.366420	r_c	0.394146
H	−0.788195	g	−0.295508
r_c^2	−0.125142	$r_c H$	0.610141
$r_c g$	0.042027	H^2	0.152965
Hg	−0.707807	g^2	0.416052
r_c^3	0.013057	$r_c^2 H$	−0.068814
$r_c^2 g$	0.000635	$r_c H^2$	−0.215558
$r_c Hg$	0.082397	$r_c g^2$	−0.083575
H^3	0.186371	$H^2 g$	0.465066
Hg^2	−0.071677	g^3	−0.007443

3.3 Regression approximation

Direct regression of α_0 is inconvenient near the no-slip limit, where a small change in the wall slip corresponds to a large change in α. Since the slip length is given by $\beta = 1/\alpha$, we introduce the dimensionless parameter

$$B = \beta / r_c = 1/\alpha r_c. \tag{25}$$

The variables r_c and g are expressed in μm in the regression below.

The FEM-calibrated solutions were treated as a supervised regression dataset, with vessel radius r_c, linear hematocrit H, and cell-free-layer thickness g as predictors and the dimensionless parameter B as the response. Polynomial feature sets of different orders were considered, and their coefficients were estimated by ordinary least squares.

Several polynomial response surfaces were tested. A cubic polynomial fitted directly to α_0 gave $R^2 = 0.803$, reflecting the strong growth of α_0 near the no-slip boundary. The same polynomial applied to $\ln \alpha_0$ improved the fit to $R^2 = 0.980$. Much smoother response surfaces were obtained for β and B. For the dimensionless variable B, the full cubic model

$$B(r_c, H, g) = \sum_{i+j+k \le 3} c_{ijk}\, r_c^i H^j g^k \tag{26}$$

gave $R^2 = 0.9998$, with RMSE $= 5.23 \cdot 10^{-4}$ and MAE $= 4.13 \cdot 10^{-4}$. Expressed in terms of the dimensional slip length β, this corresponds to an RMSE of 1.72 nm and an MAE of 1.34 nm.

The fitted coefficients are listed in Table 1. Once B is evaluated, the slip coefficient is recovered from

$$\alpha_0 = \frac{1}{r_c B(r_c, H, g)}. \tag{27}$$

The stability of the response surface was assessed by five-fold cross-validation. The resulting coefficient of determination was $R^2_{CV} = 0.9996$ and the RMSE for B was $7.02 \cdot 10^{-4}$. When converted to slip length, the cross-validated RMSE was 2.33 nm and the MAE was 1.79 nm. A fourth-order model slightly reduced the fitting error, but its cross-validated error was larger than that of the cubic model. The cubic surface was therefore retained.

Figure 5 illustrates the three-dimensional dependence of the reconstructed slip coefficient α_0 on the vessel radius, linear hematocrit, and CFL thickness predicted by the cubic model. The model is restricted to the sampled feasible domain because reconstruction of α becomes sensitive as $B \to 0$ near the no-slip limit. For the five cases with $r_c = 2.5\,\mu$m and $g = 0.5\,\mu$m, the FEM-derived values of α_0 are therefore more reliable than values reconstructed from the polynomial. The 20 geometries for which the target viscosity was not reached even under no-slip conditions are excluded from the regression.

4 Conclusion

A machine learning based polynomial surrogate approach has been developed for calibrating an effective slip boundary condition in finite-element models of blood flow in microvessels with diameters of $4-8$ μm. The required slip coefficient varies substantially with vessel radius, linear hematocrit, and CFL thickness. Of the 125 parameter combinations considered, a finite viscosity-matching value of the slip coefficient α was obtained for 105 geometries, whereas in 20 cases the FEM apparent viscosity remained below the empirical target even in the no-slip limit. The calibration therefore identifies both parameter estimates and the region in which the model can reproduce the empirical viscosity relation.

For the feasible geometries, the calibrated coefficient α varied from approximately 1.7 to 518.3 μm^{-1}. Direct finite-element calculations at all 105 estimated roots reproduced the target apparent viscosity with a mean absolute mismatch of 0.039% and a maximum mismatch of 0.136%. The dimensionless slip parameter $B = 1/\alpha r_c$ provided a smooth representation of the calibrated solutions and was accurately described by a cubic response surface, with $R^2 = 0.9998$ and a five-fold cross-validated R^2 of 0.9996.

The resulting surrogate model can be used to estimate the effective wall-slip parameter within the sampled feasible domain without repeating the full calibration procedure. Reconstruction of α becomes increasingly sensitive as B approaches zero near the no-slip limit, and direct FEM-calibrated values should therefore be preferred in this region. The calibrated slip coefficient should also be interpreted as an effective model parameter that enables the simplified continuum model to reproduce the selected empirical apparent-viscosity relation, rather than as a direct measurement of microscopic wall slip.

Ongoing work extends this framework by incorporating an additional empirical layer based on experimental measurements. This will allow the present response-surface description to be refined beyond a purely parametric representation and will enable more detailed, experimentally constrained relationships between vessel radius, hematocrit, CFL thickness, and the effective wall-slip parameter to be established and tested. In particular, the contribution of the individual model parameters and their interactions can then be examined against experimental observations. Ultimately, combining FEM calibration with experimental observations should provide a more physically constrained description of the contribution of each model parameter to microvascular flow.

Acknowledgements

The authors acknowledge support by the state of Baden-Württemberg through bwHPC and bwVisu and the German Research Foundation (DFG) through grant INST 35/1597-1 FUGG.

The work was also supported by the Ministry of Science and Higher Education of the Russian Federation (Agreement No. 075-02-2026-1312).

References

[1] N.D. Botkin, A.E. Kovtanyuk, V.L. Turova, I.N. Sidorenko, and R. Lampe. Direct modeling of blood flow through the vascular network of the germinal matrix. *Computers in Biology and Medicine*, 92:147–155, 2018.

[2] N.D. Botkin, A.E. Kovtanyuk, V.L. Turova, I.N. Sidorenko, and R. Lampe. Accounting for tube hematocrit in modeling of blood flow in cerebral capillary networks. *Comput. Math. Meth. Med.*, 2019:4235937, 2019.

[3] W. Chien, G. Gompper, and D.A. Fedosov. Effect of cytosol viscosity on the flow behavior of red blood cell suspensions in microvessels. *Microcirc.*, 28(2):e12668, 2021.

[4] A.L. Copley. Hemorheological aspects of the endothelium-plasma interface. *Microvasc. Res.*, 8(2):192–212, 1974.

[5] A.L. Copley. The endoendothelial fibrin lining, fibrinogen gel clotting, and the endothelium-blood interface. *Ann. N.Y. Acad. Sci.*, 416:377–396, 1983.

[6] P. Giri, K. Chandran, K. Muralidhar, and I. Saha Dalal. Effects of coupling of mass transport and blood viscosity models for microchannel flows. *J. Non-Newton. Fluid Mech.*, 302:104754, 2022.

[7] F. Hecht. New development in FreeFEM++. *J. Num. Math.*, 20:251–265, 2012.

[8] A. Karmakar, G.W. Burgreen, Rydquist G., and J.F. Antaki. A homogenized two-phase computational framework for meso- and macroscale blood flow simulations. *Comput. Methods Programs Biomed.*, 247:108090, 2024.

[9] A.E. Kovtanyuk, E.A. Marushchenko, and R. Lampe. The role of boundary conditions for modeling the blood flow in microvessels. *J. Phys.: Conf. Ser.*, 2514:012012, 2023.

[10] A.E. Kovtanyuk, V.L. Turova, I.N. Sidorenko, A.Y. Chebotarev, and R. Lampe. Modeling of the cerebral blood circulation in a capillary network accounting for the influence of the endothelial surface layer. *Comput. Methods Programs Biomed.*, 224:107008, 2022.

[11] C. E. McLaren, G. M. Brittenham, and V. Hasselblad. Statistical and graphical evaluation of erythrocyte volume distributions. *Am. J. Physiol. Heart Circ. Physiol.*, 252(4):H857–H866, 1987.

[12] C. Pozrikidis. Axisymmetric motion of a file of red blood cells through capillaries. *Physics of Fluids*, 17:031503, 2005.

[13] A.R. Pries, T.W. Secomb, T. Gessner, M. Sperandio, J.F. Gross, and P. Gaehtgens. Resistance to blood flow in microvessels in vivo. *Circ. Res.*, 75:904–915, 1994.

[14] A.R. Pries, T.W. Secomb, H. Jacobs, M. Sperandio, K. Osterloh, and P. Gaehtgens. Microvascular blood flow resistance: role of endothelial surface layer. *Am. J. Physiol. Heart Circ. Physiol.*, 273:H2272–H2279, 1997.

[15] Y. Rashidi, O. Aouane, A. Darras, T. John, J. Harting, C. Wagner, and S.M. Recktenwald. Cell-free layer development and spatial organization of healthy and rigid red blood cells in a microfluidic bifurcation. *Soft Matter*, 19(33):6255–6266, 2023.

[16] T.W. Secomb. Blood flow in the microcirculation. *Annu. Rev. Fluid Mech.*, 49:443–461, 2017.

[17] T.W. Secomb and A.R. Pries. Blood viscosity in microvessels: Experiment and theory. *Comptes Rendus Physique*, 14(6):470–478, 2013.